ACS OMEGA

http://pubs.acs.org/journal/acsodf

Article

CFD−PBM Simulation on Bubble Size Distribution in a Gas−Liquid−Solid Flow Three-Phase Flow Stirred Tank

Shuai Li,* Runquan Yang, Caili Wang, Hua Han, Shiyu Shen, and Huaifa Wang*

Cite This: *ACS Omega* 2022, 7, 1934−1942

Read Online

ACCESS | Metrics & More | Article Recommendations

ABSTRACT: The bubble size distribution, location distribution, and gas holdup in a gas−liquid−solid flow three-phase stirred tank were numerically simulated by the Eulerian−Eulerian method and the population balance model (PBM). The Euler−Euler method combined with the PBM model included the influence of bubble aggregation and fragmentation on the interfacial force, which can better predict the bubble size distribution and phase holdups. The simulation results show that there are some differences in the fluid morphology and gas dispersion characteristics in the stirred tank under different rotating speeds. With the increase of rotating speed, the content of small-diameter bubbles increases obviously, and they are mainly concentrated in areas with higher speeds. The higher the rotational speed, the more the bubbles with small diameters, but the content of bubbles with large diameters is less affected by the rotational speed. Small-size bubbles mainly exist in the region of high fluid velocity, while large-size bubbles mainly exist in the region of low hydrostatic pressure. Compared with the change of the bubble content at different speeds, the content of bubbles with diameters of 0.50−1.90 mm is largest at 2000 rpm, while the content of bubbles with diameters of 2.65−10.09 mm is largest at 1500 rpm. The simulation work has certain guiding significance for the research and development of the forced mineralization device and the understanding of the dispersion characteristics of bubbles in the stirred tank.

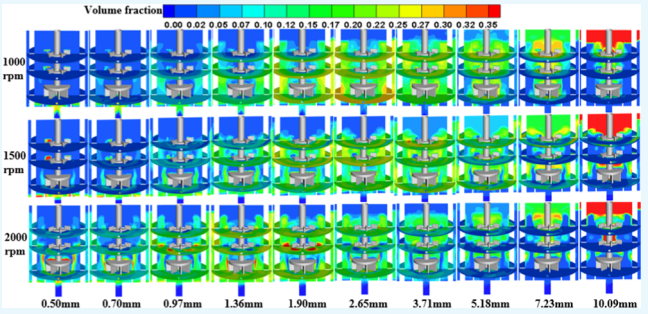

INTRODUCTION

In dispersed gas−liquid−solid three-phase flow, bubble size distribution plays an important role in the phase structure and interphase force, which determines multiphase hydrodynamic behavior. Especially in the stirred vessel with forced mixing, bubbles coalescence and break up frequently, which leads to wider range of bubble size distribution (BSD).[1] Nevertheless, this is a major unresolved problem in the gas−liquid−solid flow three-phase stirring system. The calculation of bubble size distribution and the understanding of bubble aggregation and breakage after stirring are very important for the following reasons: bubble size is significantly affected by the rotation speed, which directly affects the collision between bubble particles and solid particles. In fact, this is the mineralization stage of the flotation process, and the collision efficiency between particles needs to be strengthened. Therefore, a fluid simulation model with bubble size prediction is needed to understand foam flow.

Over the years, computational fluid dynamics (CFD) has made significant progress in the hydrodynamic behavior of the gas−liquid−solid flow multiphase. A population balance model (PBM) can predict the size distribution of bubbles and determine the average diameter of bubbles by describing the aggregation and breakage of bubbles in multiphase flow. By combining the CFD framework with PBM, a CFD−PBM coupling model is established, which not only couples the change of bubble size to the interaction between phases but also obtains the average bubble diameter and calculates the interface area and the mass transfer coefficient more accurately.[2−4] In fact, bubble coalescence and breakage occurred and the bubble sizes varied for many gas−liquid stirred tanks. In the literature, scholars such as Luo and Svendsen,[5] Prince and Blanch,[6] Lehr et al.,[7] Wang et al.,[3] and Laakkonen et al.[8] have proposed different breakage and coalescence rate models. Combining PBM with the multiphase model, the bubble size distribution and flow field in a gas−liquid stirred tank have been predicted. The simulation results are in good agreement with the experimental data. Krishna et al.[9] and Abbasi et al.[10] proposed that the hydrodynamic behaviors of a gas−liquid bubble column and a gas−solid fluidized bed are not only qualitatively but also quantitatively similar. The average bubble diameters in the two systems are

Received: September 30, 2021
Accepted: December 22, 2021
Published: January 5, 2022

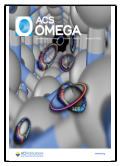

comparable, especially at low gas velocities. These results inspire the authors to study the possibility of applying the global equilibrium model (PBM) to simulate the gas−solid bubbling fluidization system. Computational simulations of the fluid flow and drop dispersion by Jasińska et al.[11] gave results that agree qualitatively with experimental data demonstrating that CFD−PBM approaches are useful for the design of high-shear rotor−stator mixers. Laakkonen et al.[8,12] predicted bubble size distribution in gas−liquid stirred tanks using the population balance model (PBM), and the simulation results are verified by the experimental data. Li et al.[13] simulated gas−liquid dispersion in a stirred tank with low and high gas loadings. Alves et al.[14] studied local average bubble sizes in aerated stirred tanks using a capillary suction probe. However, to date, there has not been a systematic simulation of the distribution position of bubbles and the relationship between bubbles of different sizes in the solid−liquid-gas three-phase flow in the stirred tank.

In this work, the size distribution and interrelationship of bubbles with different particle sizes will be simulated in the stirred tank. The PBM will be used to numerically study the interactive relationship between bubbles and bubbles, fluids, and containers at different speeds.

MATHEMATICAL MODELS

Turbulence Model. Turbulence occurs in the area where the speed changes, and it is a nonlinear complex flow. The Lagrange method and the Euler method are the two most common methods for analyzing multiphase flows. In the Euler method,[15,16] each phase can derive a set of conservation equations. The equations are closed by constitutive relations or statistical kinematics theory. The Euler method includes the volume of fluid (VOF) model, the mixture model, and the Euler model. In this work, the Euler model was used because of the high concentration of gas hydrated mineral particles.

The continuity equation of the qth phase in the Euler model is expressed as

$$\frac{\partial}{\partial t}(\alpha_q\rho_q) + \nabla\cdot(\alpha_q\rho_q\vec{v}_q) = \sum_{p=1}^{n}(\dot{m}_{qp} - \dot{m}_{pq}) + S_q \tag{1}$$

where $\vec{v}_q$, $\dot{m}_{qp}$, and $\dot{m}_{pq}$ represent the speed of the qth phase, the mass transfer from phase q to phase p, and the mass transfer from phase p to phase q, respectively. The mass transfer mechanism can be formulated separately. S_q is the source item, with its default value 0, and it can also be specified as a constant or user-defined quality source item.

The momentum equation of the qth phase in the Euler model is expressed as

$$\begin{aligned}\frac{\partial}{\partial t}(\alpha_q\rho_q\vec{v}_q) + \nabla\cdot(\alpha_q\rho_q\vec{v}_q\vec{v}_q) &= -\alpha_q\nabla p + \nabla\cdot\bar{\bar{\tau}}_q + \alpha_q\rho_q\vec{g} \\ &+ \sum_{p=1}^{n}(\vec{R}_{pq} + \dot{m}_{pq}\vec{v}_{pq} - \dot{m}_{qp}\vec{v}_{qp}) + (\vec{F}_q + \vec{F}_{lift,q} + \vec{F}_{vm,q})\end{aligned} \tag{2}$$

where $\vec{g}$ is the acceleration of gravity and $\bar{\bar{\tau}}_q$ is the stress−strain tensor of the qth phase.

$$\bar{\bar{\tau}}_q = \alpha_q\mu_q(\nabla\vec{v}_q + \nabla\vec{v}_q^{\,T}) + \alpha_q\left(\lambda_q - \frac{2}{3}\mu_q\right)\nabla\cdot\vec{v}_q\bar{\bar{I}} \tag{3}$$

where μ_q, λ_q, $\vec{F}_q$, $\vec{F}_{\mathrm{lift},q}$, $\vec{F}_{\mathrm{vm},q}$, and $\vec{R}_{pq}$ represent the shear viscosity coefficient, volume viscosity coefficient, external volume force, lift force, virtual mass force, and interphase interaction force, respectively.

The realizable $k-\varepsilon$ turbulence model introduces content related to rotation and curvature, including rotating shear flow, free flow containing jet and mixed flow, flow in a pipe, boundary layer flow, and band separation flow. It has good performance for rotating flow, boundary layer flow with strong inverse pressure gradient, flow separation, and secondary flow, so the realizable $k-\varepsilon$ model was selected in this paper. The transport equation for k and ε is expressed as

$$\frac{\partial(\rho k)}{\partial t} + \frac{\partial(\rho k u_i)}{\partial x_i} = \frac{\partial}{\partial x_j}\left[\left(\mu + \frac{\mu_t}{\partial_k}\right)\frac{\partial k}{\partial x_j}\right] + G_k - \rho\varepsilon \tag{4}$$

$$\frac{\partial(\rho\varepsilon)}{\partial t} + \frac{\partial(\rho\varepsilon u_i)}{\partial x_i} = \frac{\partial}{\partial x_j}\left[\left(\mu + \frac{\mu_t}{\partial_\varepsilon}\right)\frac{\partial\varepsilon}{\partial x_j}\right] + \rho C_1 E\varepsilon - \rho C_2\frac{\varepsilon^2}{k + \sqrt{\nu\varepsilon}} \tag{5}$$

where $\mu_t = \rho C_\mu\frac{k^2}{\varepsilon}$, $C_\mu = \frac{1}{A_0 + A_S U^* k/\varepsilon}$, and U^* is used to indicate the effect of rotation.

The virtual mass force F_V and the lift force F_L are modeled as follows[17]

$$F_V = -C_V a_g\rho_l\left(\frac{Du_g}{D_t} - \frac{Du_l}{D_t}\right) \tag{6}$$

$$F_L = -C_l a_g\rho_l(u_g - u_l)\times(\nabla\times u_l) \tag{7}$$

where C_V is the virtual mass coefficient and C_L is the lift coefficient. The theoretical value for C_L is 0.5 for a spherical bubble in a potential flow.[18] C_V strongly depends on the bubble shape and decreases with d_b.[19]

The turbulent dispersion force F_{TD} represents the force that causes the bubble movement to disperse due to turbulent pulsation.[20]

$$F_{TD} = -K_{gl}\frac{D_{gl}^t}{\omega_{gl}}\left(\frac{1}{\varnothing_l}\nabla\varnothing_l - \frac{1}{\varnothing_g}\nabla\varnothing_g\right) \tag{8}$$

where $D_{gl}^t = \frac{\mu_{t,l}}{\rho_l}$ and $\omega_l = 0.9$.

Population Balance Model. Based on the Euler model, the CFD−PBM model has the same solid−liquid model as the Euler model in three-phase flow. PBM is used to describe one or more properties of bubble, droplet, and particle swarm changing with time. As a method, the multiphase model divides the dispersed phases into categories of different sizes, where each category represents a fluid group.[21] Therefore, the model can predict the flow behavior and distribution of slurry bubbles, and then the mechanism of gas−liquid−solid flow can be further studied. From a mathematical point of view, these effects can be expressed as

$$\frac{\partial n}{\partial x} + \nabla\cdot(V_i n) + \nabla\cdot(V_e n) = B - D \tag{9}$$

$$\frac{dX}{dt} = V = V_i + V_e \tag{10}$$

https://doi.org/10.1021/acsomega.1c05406
ACS Omega 2022, 7, 1934−1942

where X is a set of internal and external coordinates(x, y, z) comprising the phase space R. By including the density, the transport equation for each class is

$$\underbrace{\frac{\partial}{\partial t}(\rho n_i)}_{\text{transient}} + \underbrace{\nabla\cdot(\rho u_e n_e)}_{\text{convective}} + \underbrace{\nabla\cdot(\rho u_i n_i)}_{\text{growth}} = \rho\underbrace{[B_B - D_B + B_C - D_C]_i}_{\text{birth and death rates}} \tag{11}$$

Birth and death rates due to breakup are expressed as

$$B_B(v; X, t) = \int_V^{V_{max}} p\beta(v/v')g(v')n(v'; X, t)\mathrm{d}v' \tag{12}$$

$$D_B(v; X, t) = g(v)\cdot n(v; X, t) \tag{13}$$

where β and g represent the probability distribution function and breakage frequency, respectively.

The aggregation kernel is given as the product of two quantizations: the frequency of the collision of particles of volumes V' and V and the probability that particles of volume V will coalesce with particles of volume V'. Birth and death rates due to coalescence are expressed as

$$B_C = \frac{1}{2}\int_0^V a(V - V')n(V - V')n(V')\mathrm{d}V' \tag{14}$$

$$D_C = \int_0^\infty a(V, V')n(V)n(V')\mathrm{d}V' \tag{15}$$

Two methods can be used to solve the population balance equation: the discrete method and the method of moment. The discrete method is adopted, which discretizes the particle population into a set of finite size intervals. Assuming that the gas phase consists of spherical bubbles with diameter L, the volume fraction of the dispersed phase can be expressed as[1]

$$\alpha_p(x, t) = \int_0^{+\infty} n(x, X, t)\frac{\pi}{6}L^3\mathrm{d}L \tag{16}$$

where the bubble state vector is represented by a set of external coordinates $(\vec{x})$, which shows the spatial position of the bubble, and X is called internal coordinates. And $n(x, X, t)$ is a number density function.

The Luo model[5] rate defines the aggregation rate as follows

$$\Omega_{ag}(V_i, V_j) = \omega_{ag}(V_i, V_j)P_{ag}(V_i, V_j) \tag{17}$$

where (ω_{ag}) is the collision frequency, which is defined as

$$\omega_{ag}(V_i, V_j) = \frac{\pi}{4}(L_i + L_j)^2 n_i n_j v_{ij} \tag{18}$$

where v_{ij} is the characteristic velocity of the collision between two bubbles with diameters of L_i and L_j. The expression is as follows

$$\vec{v}_{ij} = 1.43\varepsilon^{1/3}(L_i^{2/3} + L_j^{2/3})^{0.5} \tag{19}$$

where ε is the turbulent dissipation. P_{ag} is the probability of merging caused by collision, which can be written as

$$P_{ag} = \exp\left\{-c_1\frac{[0.75(1 + L_i^2/L_j^2)(1 + L_i^3/L_j^3)]^2}{(\rho_p/\rho_q + 0.5)^{0.5}(1 + L_i/L_j)^3}We^{0.5}\right\} \tag{20}$$

where c_1, L_i/L_j, and ρ_p/ρ_q represent a constant of order unity, the bubble size ratio, and the ratio of bubble density and liquid density, respectively.

We is the Weber number, which is defined as

$$We = \frac{\rho_q\rho_i(\vec{v}_{ij})^2}{\sigma} \tag{21}$$

where σ is the interfacial tension.

The Luo and Lehr breakage kernel breakage rate per unit volume is written as[5,7]

$$\Omega_{br}(V_i, V_j) = K\int_{\xi_{min}}^1 \frac{(1 + \xi)}{\xi^n}\exp(-b\xi^m)\mathrm{d}\xi \tag{22}$$

where parameters K, n, b, and m are reported in Table 1. ξ and f represent the dimensionless vortex size and the breakage volume fraction, respectively.

Table 1. Parameters of Both Luo and Lehr Breakage Models

	Luo	Lehr
k	$0.9238\varepsilon^{1/3}d^{-2/3}\alpha$	$1.19\varepsilon^{-1/3}d^{-7/3}\sigma\rho^{-1}f^{-1/3}$
n	11/3	13/3
b	$12(f^{2/3}+(1 - f)^{2/3}-1)\sigma\rho^{-1}\varepsilon^{-2/3}d^{-5/3}$	$2\sigma\rho^{-1}\varepsilon^{-2/3}d^{-5/3}f^{-1/3}$
m	−11/3	−2/3

Model Grid. A stirred tank with a diameter of 150 mm and a height of 200 mm was employed for simulations. The stirred tank is divided into 297 126 three-dimensional units by the structured grid method. The multiple reference frame method and the sliding grid method are two commonly used methods to cope with the stirring area in stirred reactors.

The multiple reference frame method is an approximate calculation method of the steady flow field, which uses two reference frames.[22] The rotating coordinate system is invoked as the reference system in the moving region of the agitator blade, and the static coordinate system is used in the rest regions.[23] The sliding grid method can deal with the unsteady problem,[24,25] which is the biggest difference between it and the MRF model. In a sliding grid, the relative movement between the stationary and rotating parts triggers a transient interaction effect, and the generated data is transformed and transmitted through the interface.

In this work, the sliding mesh was adopted, which is a special case of general dynamic mesh motion where the nodes move rigidly in a dynamic mesh zone. For a moving mesh with boundary motion, the integral form conservation equation of the universal scalar u on any control volume V can be written as

$$\frac{d}{dt}\int_V \rho\varphi\mathrm{d}V + \int_{\partial V}\rho\varphi((u - u_g))\cdot\mathrm{d}A = \int_{\partial V}\Gamma\nabla\varphi\cdot\mathrm{d}A + \int_V S_\varphi\mathrm{d}V \tag{23}$$

where ρ is the fluid density, $\vec{u}$ is the flow velocity vector, $\vec{u}_g$ is the mesh velocity of the moving mesh, Γ is the diffusion coefficient, and S_φ is the source term. V refers to the boundary of the control volume.

In the sliding grid, the derivative term of time can be written as

$$\frac{d}{dt}\int_V \rho\varphi\mathrm{d}V = \frac{[(\rho\varphi)^{n+1} - (\rho\varphi)^n]V}{\Delta t} \tag{24}$$

https://doi.org/10.1021/acsomega.1c05406
ACS Omega 2022, 7, 1934−1942

where n and $n + 1$ stand for the current time and the next time, respectively.

Boundary Condition. The three-fluid method in Fluent 19.0 is utilized to simulate the fluid dynamics and gas−liquid transfer characteristics of the slurry and gas in the mixing barrel (Figure 1). Gas, liquid, and solid phases are considered as

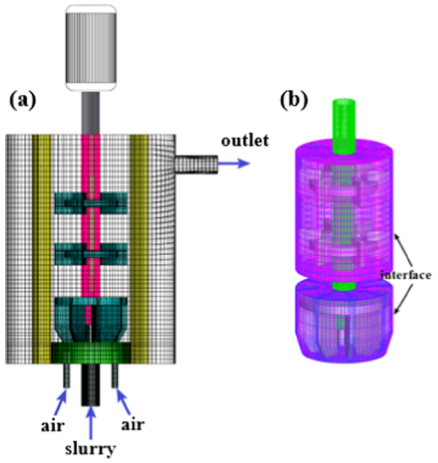

Figure 1. Three-dimensional structured grid of the stirred tank model: (a) Grid, import, and export of the stirred tank and (b) grid and interface of the rotor.

three independent pseudo-continuous phases.[26] The liquid phase is an ongoing primary phase, and the gas and solid phases are dispersed secondary phases. The pressure and viscosity of dispersed solids are simulated by granular flow theory.[27] In the computational domain, three phases are interpenetrating and interacting.

The parameters of the working conditions were as follows: the inlet velocity of the slurry was 0.264 m/s; the velocities of the two air inlets were both 0.594 m/s; the solid particles were coal with a density of 1400 kg/m^3, a solid particle size of 0.1 mm, and a slurry concentration of 80 g/L. The major project of this work is to study the bubble size, the range of which is subdivided into 10 groups. The velocity inlet boundary was adopted at the inlet of the model and the pressure outlet boundary was adopted at the outlet. The default parameter setting of 5% turbulence intensity was fixed at the entrance of air and slurry, and their actual diameter was set as the hydraulic diameter. Under-relaxation factors were set to 0.3 for pressure and momentum, 0.5 for the volume fraction, and 0.8 for turbulent kinetic energy, turbulent dissipation rate, and turbulent viscosity. A time step of 0.001 s with 20 iterations per time step was used, and all residual values were set to 0.001 as the convergence criterion. Besides, more details of the simulation setting are presented in Table 2.

RESULTS AND DISCUSSION

Flow Field Analysis. As shown in Figure 2, the flow field is studied by the contours or data on five cut planes (P1−P5) and two straight lines (L1−L2), mainly including the fluid characteristics of the solid−liquid−gas three phase, especially the data characteristics of the gas phase. Figure 3 shows the velocity vector diagram of the P1 surface under different speed conditions. It can be observed that there are more vortices generated by the fluid at 1500 rpm speed. Vortex can cause the bubble to break and make the solid particles involved and gathered.

Table 2. Simulation Settings in a Gas−Liquid−Solid Flow Stirred Tank

granular viscosity	Gidaspow
granular bulk viscosity	Lun et al.
frictional viscosity	Schaeffer
granular temperature	algebraic
solid pressure	Lun et al.
radial distribution	Lun et al.
rotation domain	mesh motion
pressure−velocity coupling	phase coupled SIMPLE
spatial discretization momentum	second-order upwind
spatial discretization volume fraction	QUICK
spatial discretization turbulent kinetic energy	first-order upwind
spatial discretization turbulent dissipation rate	first-order upwind
spatial discretization air bin	first-order upwind
surface tension in the Luo and Lehr models	0.71
critical weber number in the Lehr model	0.1

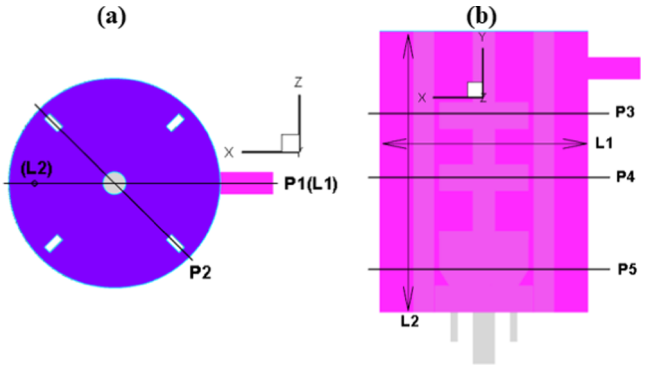

Figure 2. Schematic diagram of the position of the cut plane and the straight line: (a) XZ plane coordinate view and (b) XY plane coordinate view.

Based on the Euler model, Figure 4 shows the contours of the speed change, static pressure change, turbulent dissipation rate change, and coal volume fraction change in the stirred tank at different rotation speeds. With the increase of the rotating speed, the velocity range of the fluid increases gradually, and the velocity near the impeller is highest. The pressure in the upper part of the drum and the center of the impeller is smaller, especially the higher the rotating speed, the more noticeable this phenomenon. With the increase of rotating speed, the volume fraction of coal in the mixing drum decreases gradually, which means that the higher the rotating speed, the higher the average velocity of coal particles and the shorter the residence time in the drum.

Distribution of the Bubble Volume Fraction. Figure 5 shows the distribution of the bubble volume fraction of different particle sizes on the cut planes (P2−P5) at different rotational speeds. With the increase of rotating speed, the content of small-diameter bubbles increases obviously, and they are mainly concentrated in areas with higher speeds. The higher the rotating speed, the more obvious the turbulence of the liquid phase, and the greater the bubble breaking effect. Regardless of the rotation speed, the content of large-diameter bubbles is obviously higher, and they are mainly concentrated in areas with lower static pressure.

Statistical Analysis of Bubble Size. Figure 6 shows the number density of bubbles with different particle sizes at different rotating speeds. Regardless of the rotation speed, the

https://doi.org/10.1021/acsomega.1c05406
ACS Omega 2022, 7, 1934−1942

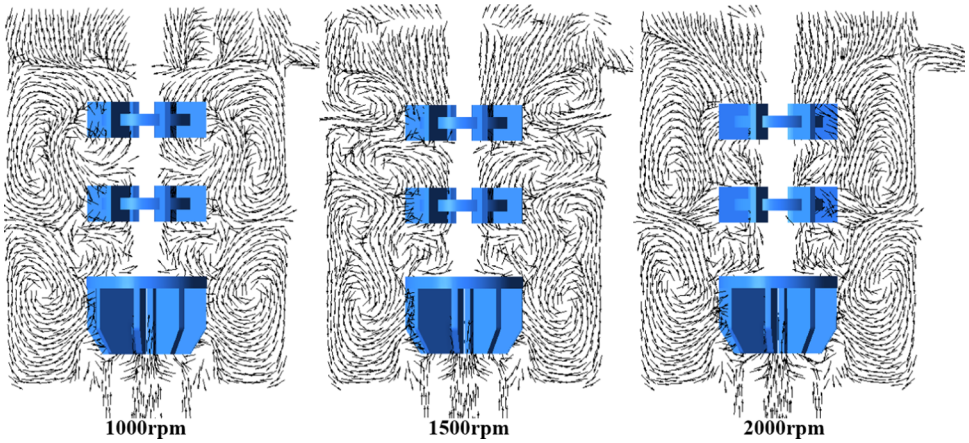

Figure 3. Speed vector diagram of the P1 surface at different speeds.

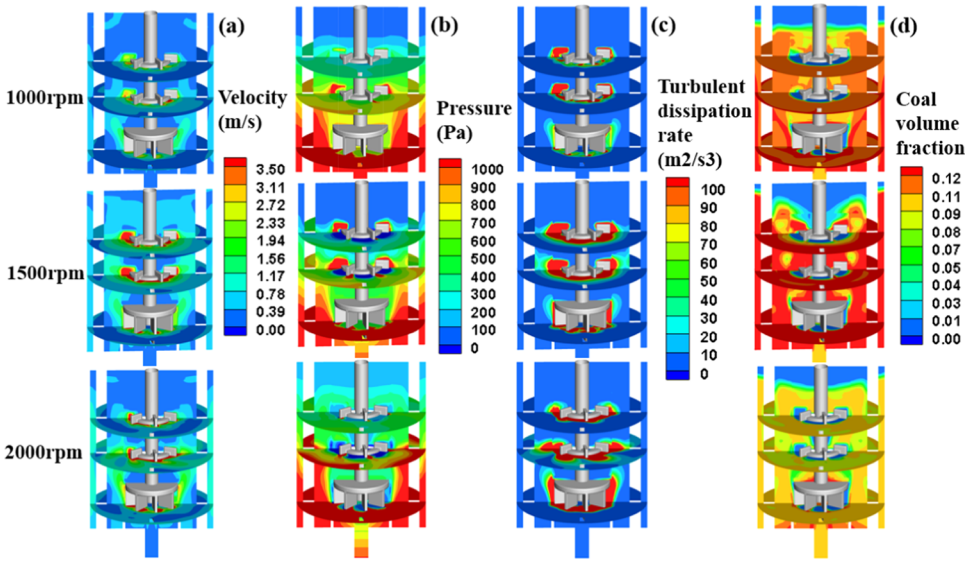

Figure 4. Contours of the speed change (a), static pressure change (b), turbulent dissipation rate change (c), and coal volume fraction change (d).

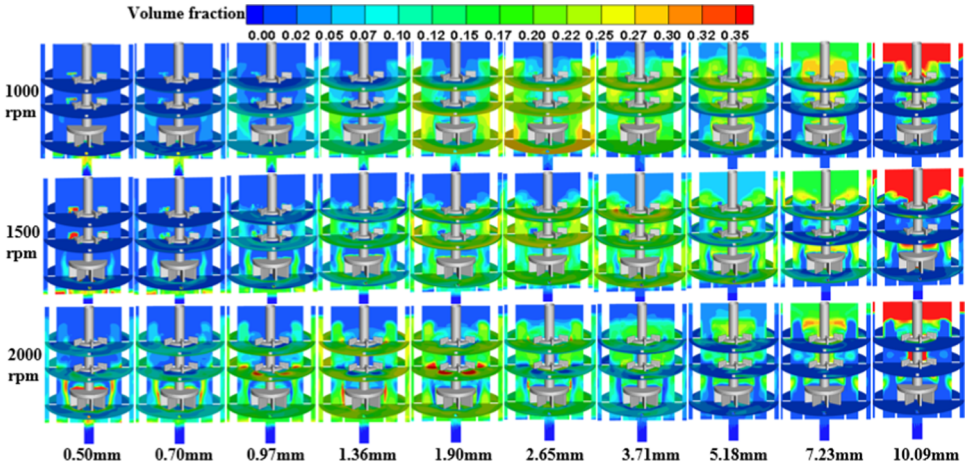

Figure 5. Gas holdup distribution of bubbles with different particle sizes at different speeds.

particle number density of small-diameter bubbles is obviously higher, and the smaller the diameter, the greater the particle number density. The particle number density of bubbles with diameters of 0.50−1.90 mm is the maximum at a rotation speed of 2000 rpm, while the particle number density of bubbles with diameters of 2.65−10.09 mm is the maximum at a rotation speed of 1500 rpm. Comparing the results of the rotation speed conditions of 1000 and 2000 rpm, the particle number density of bubbles with diameters of 0.50−2.65 mm is greater for the latter, while the particle number density of

https://doi.org/10.1021/acsomega.1c05406
ACS Omega 2022, 7, 1934−1942

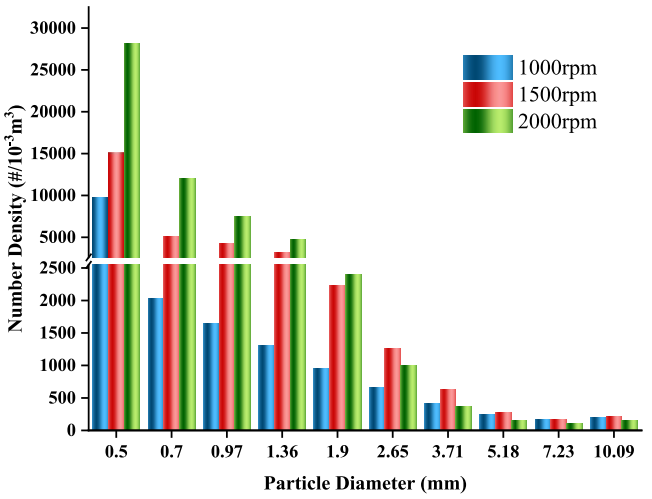

Figure 6. Particle number density of bubbles with different particle sizes at different rotating speeds.

bubbles with diameters of 3.71−10.09 mm is greater for the former. Comparing the results of the speed conditions of 1000 and 1500 rpm, the particle number density of bubbles in all diameter ranges is larger for the latter.

Figure 7 shows the volume density and proportion of bubbles with different particle sizes at different rotating speeds. Regardless of the rotation speed, the larger the diameter, the greater the volume density of the bubbles. Comparing the results from different speed conditions, the change trend of the volume density of all bubbles in the diameter range is completely the same as the change trend of the particle number density. From the proportion of each diameter bubble in total gas volume, with the increase of diameter, the proportion first increases slowly and then increases rapidly. This happens because the CFD−PBM model treats the gas gathered in the low-pressure area as large-diameter bubbles, such as bubbles with a diameter of 10.09 mm.

Figure 8 shows the surface area density and proportion of bubbles with different particle sizes at different rotating speeds. The surface area density of bubbles with diameters of 0.50−1.90 mm is the maximum at a rotation speed of 2000 rpm, while the density of bubbles with diameters of 2.65−10.09 mm is the maximum at a rotation speed of 1500 rpm. Comparing the results of the rotation speed conditions of 1000 and 2000 rpm, the surface area density of bubbles with diameters of 0.50−2.65 mm is greater for the latter, while the density of bubbles with diameters of 3.71−10.09 mm is greater for the former. Comparing the results of the speed conditions of 1000 and 1500 rpm, the surface area density of bubbles in all diameter ranges is larger for the latter. From the proportion of each diameter bubble in the total gas volume, with the increase of diameter, the proportion no longer increases in one direction but fluctuates.

Effect of Fluid Behavior. Figure 9 shows the relationship between some bubbles and fluid behavior on line L1. There is a positive correlation between fluid velocity and the turbulent dissipation rate. The volume fraction of bubbles with diameters of 1.36 and 5.18 mm are opposite to each other along the *x*-axis. The content of bubbles with a diameter of 10.09 mm in the center of the *x*-axis is much greater than those at other positions, which is exactly the opposite of the static pressure value. The content of bubbles with a diameter of 0.70 mm increases slowly with the increase of fluid speed. The content of bubbles with a diameter of 2.65 mm has a positive correlation with static pressure at 1000 rpm, with a positive correlation with the fluid velocity at 1500 rpm, and without obvious regularity at 2000 rpm.

Figure 10 shows the relationship between some bubbles and fluid behavior on line L2. The static pressure decreases along the *y*-axis. The fluid velocity value and the turbulent dissipation rate value are still positively correlated. The volume fraction of bubbles with diameters of 1.36 and 5.18 mm still shows the opposite relationship along the *y*-axis. The content of bubbles with a diameter of 10.09 mm suddenly increases at some positions along the *y*-axis at a speed of 1500 rpm, especially the position where the static pressure is lowest. The content of bubbles with a diameter of 0.70 mm is obviously higher at the position where the static pressure is highest and increases slowly with the increase of fluid velocity at other positions. The

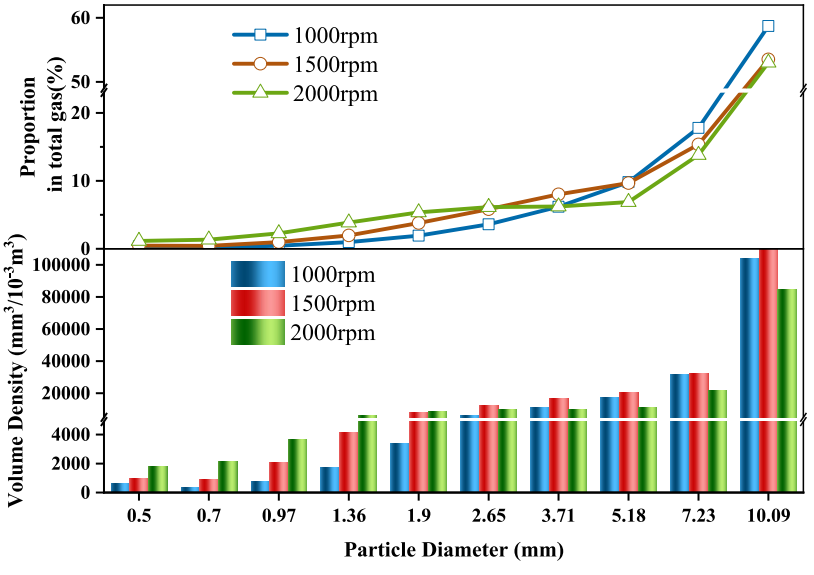

Figure 7. Volume density and proportion of bubbles with different particle sizes at different rotating speeds.

https://doi.org/10.1021/acsomega.1c05406
ACS Omega 2022, 7, 1934−1942

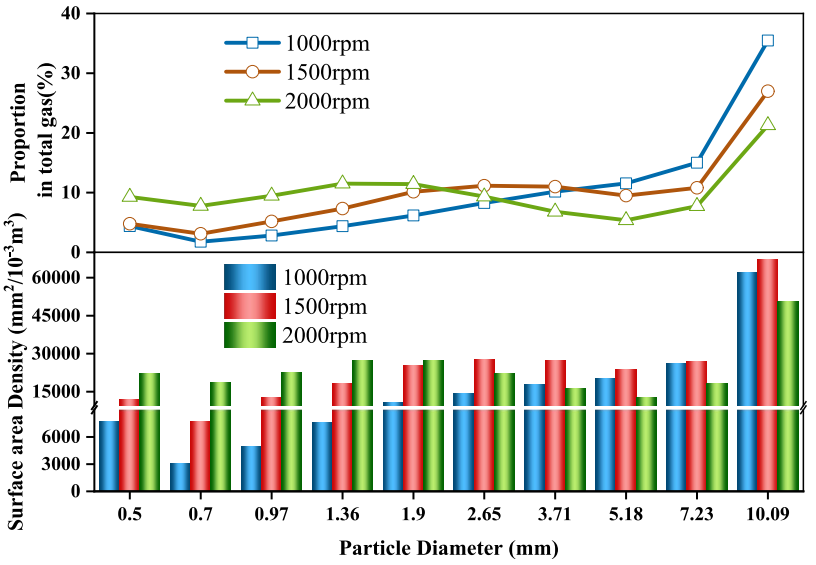

Figure 8. Surface area density and proportion of bubbles with different particle sizes at different rotating speeds.

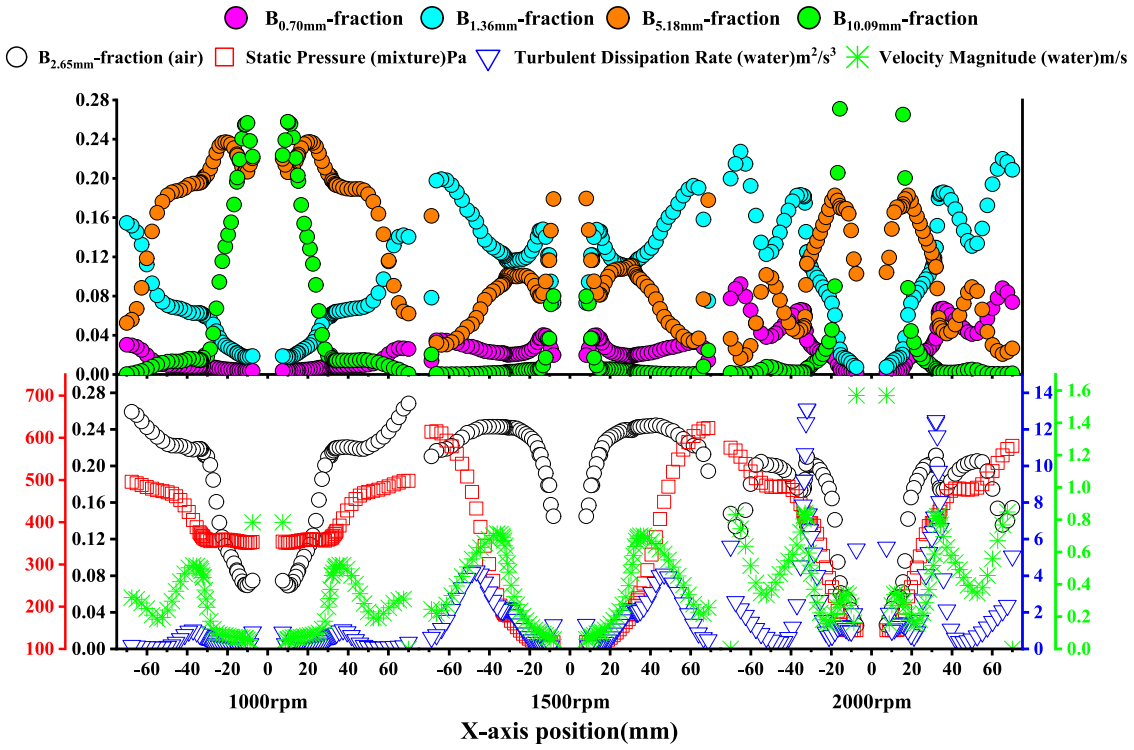

Figure 9. Relationship between some bubbles and fluid behavior on line L1.

content of bubbles with a diameter of 2.65 mm has no obvious law along the *y*-axis.

CONCLUSIONS

In this study, a relatively comprehensive Eulerian three-phase model coupled with the PBM was established, and the distribution of the gas volume fraction, statistical analysis of bubble size, flow field analysis, and effect of fluid behavior were realized. The realizable $k-\varepsilon$ turbulence model was used to simulate the complex fluid flow in the stirred tank at different speeds. The size distribution and statistics of the bubbles were studied under different rotation speeds. The following conclusions can be drawn

(1) The fluid velocity near the impeller is highest, and the pressure in the upper part of the mixing drum and the center of the impeller is lower. With the increase of rotating speed, the volume fraction of coal in the mixing drum decreases gradually.

(2) The number density, volume density, and surface area density of bubbles with diameters of 0.50−1.90 mm are largest at a speed of 2000 rpm, while the number density, volume density, and surface area density of bubbles with diameters of 2.65−10.09 mm are largest at a speed of 1500 rpm.

(3) The contents of bubbles with diameters of 1.36 and 5.18 mm always exhibit an opposite relationship along the *x*-

https://doi.org/10.1021/acsomega.1c05406
ACS Omega 2022, 7, 1934−1942

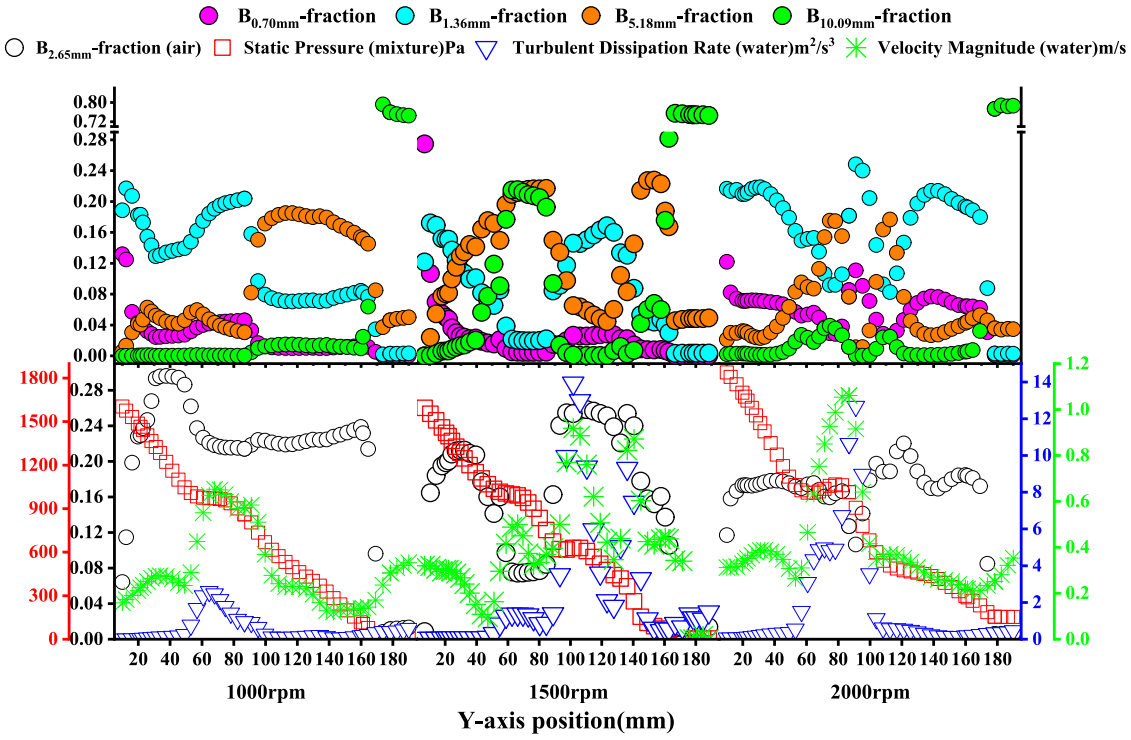

Figure 10. Relationship between some bubbles and fluid behavior on line L2.

or *y*-axis. Bubbles with a diameter of 0.70 mm mainly appear in areas where the fluid velocity is higher, while bubbles with a diameter of 10.09 mm mainly appear in areas where the static pressure is lowest. Bubbles with a diameter of 2.65 mm did not show obvious regularity.

AUTHOR INFORMATION

Corresponding Authors

Shuai Li − *College of Mining Engineering, Taiyuan University of Technology, Taiyuan 030024 Shanxi, China;* orcid.org/0000-0001-5784-0949; Email: lishuailsls@163.com

Huaifa Wang − *College of Mining Engineering, Taiyuan University of Technology, Taiyuan 030024 Shanxi, China; State Key Laboratory of Mineral Processing, Beijing 100160, China*; Email: wanghuaifa@tyut.edu.cn

Authors

Runquan Yang − *College of Mining Engineering, Taiyuan University of Technology, Taiyuan 030024 Shanxi, China*

Caili Wang − *College of Mining Engineering, Taiyuan University of Technology, Taiyuan 030024 Shanxi, China*

Hua Han − *College of Mining Engineering, Taiyuan University of Technology, Taiyuan 030024 Shanxi, China*

Shiyu Shen − *College of Mining Engineering, Taiyuan University of Technology, Taiyuan 030024 Shanxi, China*

Complete contact information is available at: https://pubs.acs.org/10.1021/acsomega.1c05406

Author Contributions

The manuscript was written through contributions of all authors. All authors have given approval to the final version of the manuscript.

Notes

The authors declare no competing financial interest.

ACKNOWLEDGMENTS

This work was funded by Open Foundation of State Key Laboratory of Mineral Processing, Grant No. BGRIMM-KJSKL-2020-14.

REFERENCES

(1) Li, L.; Liu, Z.; Li, B.; Matsuura, H.; Tsukihashi, F. Water Model and CFD-PBM Coupled Model of Gas-Liquid-Slag Three-Phase Flow in Ladle Metallurgy. *ISIJ Int.* **2015**, *55*, 1337−1346.

(2) Liang, X. F.; Pan, H.; Su, Y. H.; Luo, Z. H. CFD-PBM approach with modified drag model for the gas−liquid flow in a bubble column. *Chem. Eng. Res. Des.* **2016**, *112*, 88−102.

(3) Wang, T.; Wang, J.; Yong, J. A CFD−PBM coupled model for gas−liquid flows. *AICHE J.* **2006**, *52*, 125−140.

(4) Wang, T.; Wang, J. Numerical simulations of gas−liquid mass transfer in bubble columns with a CFD−PBM coupled model. *Chem. Eng. Sci.* **2007**, *62*, 7107−7118.

(5) Luo, H.; Svendsen, H. F. Theoretical model for drop and bubble breakup in turbulent dispersions. *AIChE J.* **1996**, *42*, 1225−1233.

(6) Prince, M. J.; Blanch, H. W. Bubble Coalescence and Break-Up in Air-Sparged Bubble Columns. *AIChE J.* **1990**, *36*, 1485−1499.

(7) Lehr, F.; Millies, M.; Mewes, D. Bubble-Size Distribution and Flow Fields in Bubble Columns. *AIChE J.* **2002**, *48*, 2426−2443.

(8) Laakkonen, M.; Alopaeus, V.; Aittamaa, J. Validation of bubble breakage, coalescence and mass transfer models for gas−liquid dispersion in agitated vessel. *Chem. Eng. Sci.* **2006**, *61*, 218−228.

(9) Krishna, R.; et al. Analogous description of the hydrodynamics of gas-solid fluidized beds and bubble columns. *Chem. Eng. J. Biochem. Eng. J.* **1993**, *53*, 89−101.

(10) Abbasi, M.; et al. Numerical comparison of gas-liquid bubble columns and gas-solid fluidized beds. *Can. J. Chem. Eng.* **2015**, *93*, 1838−1848.

(11) Jasińska, M.; et al. Dispersion of oil droplets in rotor-stator mixers: Experimental investigations and modeling. *Chem. Eng. Process.: Process Intensif.* **2014**, *84*, 45−53.

(12) Laakkonen, M.; Moilanen, P.; Alopaeus, V.; Aittamaa, J. Modelling local bubble size distributions in agitated vessels. *Chem. Eng. Sci.* **2007**, *62*, 721−740.

https://doi.org/10.1021/acsomega.1c05406
ACS Omega 2022, 7, 1934−1942

(13) Li, L.; Ning, C.; Xiang, K.; Xiang, B. A Comparative CFD Study on Gas-Liquid Dispersion in A Stirred Tank with Low and High Gas Loadings. *Int. J. Chem. React. Eng.* **2018**, *16*, 1−21.
(14) Alves, S. D. S.; Maia, C. I.; Vasconcelos, J. M. T.; Serralheiro, A. J. Bubble size in aerated stirred tanks. *Chem. Eng. J.* **2002**, *89*, 109−117.
(15) Chou, Y.-J.; Wu, F.-C.; Shih, W.-R. Toward numerical modeling of fine particle suspension using a two-way coupled Euler-Euler model: Part 2: Simulation of particle-induced Rayleigh-Taylor instability. *Int. J. Multiphase Flow* **2014**, *64*, 44−54.
(16) Chou, Y.-J.; Wu, F.-C.; Shih, W.-R. Toward numerical modeling of fine particle suspension using a two-way coupled Euler-Euler model. Part 1: Theoretical formulation and implications. *Int. J. Multiphase Flow* **2014**, *64*, 35−43.
(17) Minev, P. D.; Lange, U.; Nandakumar, K. A comparative study of two-phase flow models relevant to bubble column dynamics. *J. Fluid Mech.* **1999**, *394*, 73−96.
(18) Auton, T. R. The Lift Force on a Spherical Body in Rotational Flow. *J. Fluid Mech.* **1987**, *183*, 199−218.
(19) Tomiyama, A.; Sou, A.; Zun, I.; Kanami, N.; Sakaguchi, T. Effects of Eötvös Number and Dimensionless Liquid Volumetric Flux on Lateral Motion of a Bubble in a Laminar Duct Flow. *Multiphase Flow* **1995**, *1995*, 3−15.
(20) Burns, A. D.; Frank, T.; Hamill, I.; Shi, J. M. In *The Favre Averaged Drag Model for Turbulent Dispersion in Eulerian Multi-Phase Flows*, 5th ICMF'04, 2004.
(21) Buffo, A.; Vanni, M.; Marchisio, D. L. Multidimensional population balance model for the simulation of turbulent gas-liquid systems in stirred tank reactors. *Chem. Eng. Sci.* **2012**, *70*, 31−44.
(22) Issa, R.; Luo, J. Y.; Gosman, D. In *Prediction of Impeller Induced Flows in Mixing Vessels using Multiple Frames of Reference*, 4th European Conference on Mixing, IMechE Symposium Series, 1994.
(23) Lane, G. L.; Schwarz, M. P.; Evans, G. M. In *Comparison of CFD Methods for Modelling of Stirred Tanks*, 10th European Conference on Mixing, 2000; pp 273−280.
(24) Jahoda, M.; Moštěk, M.; Kukuková, A.; Machoň, V. CFD Modelling of Liquid Homogenization in Stirred Tanks with One and Two Impellers Using Large Eddy Simulation. *Chem. Eng. Res. Des.* **2007**, *85*, 616−625.
(25) Jaworski, Z.; Bujalski, W.; Otomo, N.; Nienow, A. W. CFD Study of Homogenization with Dual Rushton Turbines—Comparison with Experimental Results: Part I: Initial Studies. *Chem. Eng. Res. Des.* **2000**, *78*, 327−333.
(26) Zhou, X.; Ma, Y.; Liu, M.; Zhang, Y. CFD-PBM simulations on hydrodynamics and gas-liquid mass transfer in a gas-liquid-solid circulating fluidized bed. *Powder Technol.* **2020**, *362*, 57−74.
(27) Lewis, W. K.; Whitman, W. G. Principles of Gas Absorption. *Ind. Eng. Chem.* **1924**, *16*, 1215−1220.

https://doi.org/10.1021/acsomega.1c05406
ACS Omega 2022, 7, 1934−1942